1993ApJ...409..705H

THE ASTROPHYSICAL JOURNAL, 409:705–719, 1993 June 1
© 1993. The American Astronomical Society. All rights reserved. Printed in U.S.A.

THE FORMATION AND EVOLUTION OF SHOCKS IN STELLAR JETS FROM A VARIABLE WIND

PATRICK HARTIGAN
Five College Astronomy Department, University of Massachusetts, Amherst, MA 01003
AND
JOHN RAYMOND
Harvard-Smithsonian Center for Astrophysics, Mail Stop 16, 60 Garden Street, Cambridge MA 02138
Received 1992 July 24; accepted 1992 November 30

ABSTRACT

Recent observations of jets from young stars indicate that the bright emission knots in these jets form at least in part because the jet varies in velocity and produces low-velocity shocks in the flow. In this paper we use a one-dimensional fluid dynamics code that includes detailed cooling by line emission to investigate how shocks develop and evolve in a variable wind. Supersonic velocity perturbations in a jet always steepen and form a pair of shocks (called the "forward" and "reverse" shocks), which separate gradually as the flow evolves. Line emission from the hot gas between these shocks has a low-excitation spectrum and large radial and tangential motions with respect to the exciting source, in agreement with observations of stellar jets.

The forward shock has a larger shock velocity than the reverse shock if a density enhancement accompanies the velocity perturbation. If there is no initial density perturbation then the forward and reverse shocks have equal shock velocities, and if the density perturbation is negative (corresponding to constant mass loss) then the reverse shock has a larger shock velocity. In all cases except the constant mass-loss scenario the forward shock radiates more [S II] $\lambda\lambda$6716, 6731 emission than the reverse shock because the material that encounters the reverse shock must first pass through a rarefaction wave.

The total [S II] emission produced by modest ($\sim$40 km s^{-1}) velocity perturbations rises rapidly as the shocks develop, and then either increases or decreases gradually (depending on the size of the perturbation) over tens of years. Models with strong magnetic fields have lower line fluxes and lower excitation than models without fields, and the perturbations disperse more rapidly if a magnetic field is present. Knots from variable stellar jets show how much the stellar winds change over time scales of $\sim$10 years.

Subject headings: hydrodynamics — ISM: jets and outflows — shock waves — stars: mass loss — stars: pre–main-sequence

1. INTRODUCTION

Stellar jets play an important role in the evolution of most young stars. These highly collimated flows may be the primary way that a young star loses the angular momentum that it gains when it accretes material from a dense circumstellar disk (Edwards, Ray, & Mundt 1993). If the jets are mostly neutral they could also provide sufficient momentum and energy to drive molecular outflows and dissipate the surrounding molecular cloud. Stellar jets radiate forbidden lines, so it is possible to measure the electron densities, excitation conditions, and kinematics of these flows directly, which is not true for many astrophysical jets. Observations of jets from young stars indicate how hydrodynamical models of jets in general can be improved, and also provide critical information about the exciting source such as mass-loss rates and variability.

Recent detailed observations of the line emission from stellar jets have enabled several groups (e.g., Morse et al. 1992; Reipurth & Heathcote 1991) to separate the emission at the end of the jet into a component from the bow shock and a component from the Mach disk. Although planar shock models often do not explain some of the details of these flows, the presence of two radiative shocks, the Mach disk and the bow shock, at the heads of stellar jets agrees with predictions from simple theoretical models (Hartigan 1989). In contrast, the high velocity "knots" of shock-excited emission within stellar jets could in principle arise from any of a number of mechanisms that form weak shocks in jets such as reflection modes, cooling, external density gradients, and pressure from a backflowing cocoon (Blondin, Königl, & Fryxell 1989; Falle, Innes, & Wilson 1987; Raga, Binette, & Canto 1989; Wilson & Falle 1985; Norman, Smarr, & Winkler 1985). However, most of these mechanisms fail to produce large proper motions, low excitation spectra, and close spacings of the emission knots in stellar jets (e.g., Reipurth 1989).

One model for the knots in stellar jets that agrees with the observations and is also plausible on physical grounds is a jet that varies in velocity. The accretion rates through disks around T Tauri stars (the energy sources that probably drive stellar jets) sometimes vary by factors of 2 in 24 hours (Hartigan et al. 1991). Probably all of these disks occasionally accrete at much higher rates during "FU Ori" and "EXOR" outbursts (Hartmann, Kenyon, & Hartigan 1993; Eislöffel et al. 1991), and these episodic accretion events could produce massive ejections every 100–1000 years along stellar jets. Direct evidence for young stellar winds that vary on time scales of months comes from high-velocity absorption features in line profiles of NaD in many T Tauri stars (Mundt 1984). Large wind variations on time scales of $\sim$1000 years produce bow shocks that move into the wakes of previous ejections from the central sources (HH 111—Reipurth, Raga, & Heatcote 1992; HH 47—Hartigan, Raymond, & Meaburn 1990; HH 34—Morse et al. 1992).

© American Astronomical Society • Provided by the NASA Astrophysics Data System

1993ApJ...409..705H

A wind that varies supersonically, in velocity will produce shock waves along the outflow as the fast wind overtakes the slower wind. Although this phenomenon must occur in stellar jets, there has been little work to date that quantifies how velocity variability translates into shock-excited gas along a stellar jet. An analytical model for the positions of velocity discontinuities in a variable jet has been investigated using Burgers's equation by Raga et al. (1990), and Raga & Kofman (1992). However, Burgers's equation neglects all pressure forces, so this approach cannot describe how the velocity and density profiles in a variable wind change with time, and cannot provide any quantitative information about line emission from a variable wind. Shocks produced by coronal mass ejections in a variable velocity solar wind have recently been modeled by Whang (1991), but these simulations are not directly relevant to stellar jets because they lack radiative cooling.

In this paper we calculate one-dimensional hydrodynamical simulations of a variable jet that include detailed cooling by line emission. In § 2 we review the basic physics that determined how variable winds evolve, and we also summarize the numerical method used in the models. In § 3 we show that a supersonic velocity perturbation in a wind produces a pair of shocks, and we calculate the line fluxes from the gas heated by the shock waves. We also consider how magnetic fields, density perturbations, and different shapes for the initial velocity perturbations affect the evolution of a variable jet, and we investigate how observations of knots in stellar jets constrain the time scales of the variability of young stellar winds. The principal conclusions from our study are summarized in § 4. Contemporaneously with our work, Stone & Norman (1993) have derived similar results from their numerical simulations of periodic jets. The Stone & Norman models are two-dimensional, but use somewhat less detailed cooling than the models we present in this paper.

2. OVERVIEW OF THE MODEL

2.1. *Basic Physics, Goals, Limitations*

The basic physics that governs the formation and evolution of shocks in a velocity variable wind also describes the evolution of velocity and density profiles in sound waves (e.g., Landau & Lifshitz 1959). In both cases the portions of the flow with the largest velocities also have the largest sound speeds, so the velocity profile of a wave steepens and eventually forms a shock. The formation of shocks does not happen in linear theory; the velocity and density profiles of waves in linear theory remain fixed in time because the sound speed is constant for all portions of the wave.

If the velocity perturbation is supersonic, as will often be the case in stellar jets, then a pair of shocks must form as the velocity perturbation steepens. In this paper we refer to the shock at the greatest distance from the exciting source as the "forward" shock, and the shock closest to the exciting source as the "reverse" shock. The forward shock moves into the undisturbed ambient medium in front of the perturbation, and the reverse shock slows the fast material from the velocity perturbation. An imperfect, but compelling analogy is that of the multiple car accident that would form as a stream of fast vehicles rams into a column of slower moving vehicles. In this case the "forward" shock occurs where the slow vehicles are being rammed from behind, and the "reverse" shock occurs where the fast vehicles overtake the accident. Similar forward and reverse shocks also appear at the head of the stellar jet as the bow shock and Mach disk, respectively, and in supernova remnants (McKee 1974).

The primary goal of the models in this paper is to illustrate the basic physics involved when a velocity wave steepens to form a pair of shocks. We want to determine whether or not both shocks will be visible, and estimate the rise and decay times of the emission from the shocks. We also wish to investigate how a strong magnetic field affects the formation and evolution of shocks in jets. Because the model is one-dimensional, we cannot follow the morphology of the bow-shock/Mach-disk structure that will form from this process (see Wilson 1984 and Stone & Norman 1993 for a discussion of the two-dimensional structure of shocks formed in a variable jet), but we can calculate the radiative cooling in more detail than is currently possible in two-dimensional simulations. Material between the two shocks will flow to the side on a time scale of the sound crossing time, which for stellar jets is $\sim 5 \times 10^9$ seconds. For this reason our models only follow the evolution of the flow for $\sim 10^9$ seconds. The primary difference between our one-dimensional results and the two-dimensional models of Stone & Norman is that the two-dimensional simulations produce bow shocks instead of planar shocks.

2.2. *The Numerical Code and the Cooling*

The numerical simulation is based on the one-dimensional hydrodynamical code developed by Yahil, Johnston, & Burrows (1985). This code uses a Godunov scheme with parabolic spatial accuracy (spatial accuracy is important in rarefaction waves), and conserves momentum, mass, and energy implicitly (see the Appendix in Falle 1991, for a discussion of modern numerical methods for capturing shocks). Shocks captured in Gudunov methods are only 1–2 zones wide, and this spatial precision can be important for determining the cooling in the postshock portions of the flow (the cooling from collisional excitation and ionization of neutral hydrogen depends exponentially on the temperature of the gas). The model uses a predictor-corrector to advance forward in time, and the time advancement uses Lagrangian variables which are remapped to Eulerian coordinates after the time step is complete. We tested the model by applying it to a Sedov blast wave problem and a solar wind problem, and in both cases the model converged to the analytical solution. Further details of the numerical method appear in Appendix A.

Because the model is one-dimensional, it is possible to consider detailed cooling. The cooling is calculated between the predictor and corrector steps, and the time step is reduced if the cooling radiates more than 2% of the internal energy in any cell during the time step. We ignore photoionization, but include collisional excitation and de-excitation, collisional ionization, radiative decay, and recombination for nine elements. The ionization of H is recalculated every time step from the ionization and recombination rate coefficients. We assume that the ionization of N and O are tied to that of H through charge exchange. He is neutral in the model, and the elements C, S, Si, Fe, and Mg are singly ionized everywhere.

The preceding assumptions regarding the ionization states are appropriate for interstellar gas between 10^3 K and $\sim 4 \times 10^4$ K, and for shock waves that heat neutral gas to $\lesssim 8 \times 10^4$ K. Shock waves in neutral gas with postshock temperatures $\lesssim 8 \times 10^4$ K cool before the gas becomes doubly ionized. The cooling rate includes the H and He resonance lines and the 13 strongest forbidden lines. Density sensitivity is

© American Astronomical Society • Provided by the NASA Astrophysics Data System

1993ApJ...409..705H

included through an approximation to the two-level results. We assume that the electron and ion temperatures are equal everywhere.

2.3. *Initial Conditions*

We begin the model with a velocity perturbation (usually Gaussian or triangular) which is sometimes accompanied by a similar density perturbation. The initial H ionization fraction is taken to be 0.01. The electron densities and the total amount of line emission increase if the initial H ionization function is increased, but the evolution of the shocks in the jet does not depend upon the initial H ionization. The velocity outside of the perturbation is 10 km s^{-1}, which makes the profile drift gradually from left to right during the simulation. The simulation covers only a small section ($\delta r/r \ll 1$) of the jet, so effects of free expansion are negligible. We adopt a jet radius of 2.4×10^{15} cm, which yields a jet diameter of 0".7 at 460 pc (similar to the diameter of the jet in HH 34, Bührke, Mundt, & Ray 1988). The abundances of H:He:C:N:O:Mg:Si:S:Fe used in the model are $1{:}0.1{:}3 \times 10^{-4}{:}10^{-4}{:}6 \times 10^{-4}{:}2 \times 10^{-5}{:}4 \times 10^{-5}{:}4 \times 10^{-5}$. Our choices for the densities and the amplitude of the velocity perturbations in our models were motivated by the observed line ratios of the stellar jets in HH 111 (Reipurth 1989) and HH 34 (Reipurth et al. 1986).

3. RESULTS

Table 1 shows the initial conditions for seven models of jet variability. Model A initially has a Gaussian velocity perturbation and constant density everywhere. In model B we accompany the velocity perturbation with a similar Gaussian density enhancement, and in model C the density is diminished in the perturbation so that ρv is constant everywhere. The velocity perturbations are all Gaussian-shaped, except for model D which has a triangular-shaped perturbation. Model E uses a lower (25 km s^{-1}) perturbation, model F has a transverse magnetic field of 0.5 mG everywhere, and the perturbation in model G is 50% wider than the perturbations in models A, B, C, and E.

Because our models are one-dimensional, we can add an arbitrary constant to the model velocities to obtain the velocity of the material with respect to the star. A similar constant can be applied to the radius scale on the x-axis. In the models displayed below, the sound speed and the velocity have units of km s^{-1}, the density is in units of cm^{-3}, and the [S II] emissivity ($\lambda 6716 + \lambda 6731$) has units of 10^{-16} ergs cm^{-3} s^{-1}. A sound speed of 10 km s^{-1} corresponds to a temperature of $\sim 10^4$ K. Each cell subtends 0.5 AU, so the total flux from each cell seen at the Earth is given by [5.3×10^{-16}(emissivity/10^{-16} ergs cm^{-3} s^{-1})] ergs cm^{-2} s^{-1}, for a jet radius of 2.4×10^{15} cm and a distance of 460 pc.

TABLE 1

PARAMETERS OF VARIABLE JET MODELS

Model	Perturbation Δv (km s^{-1})	Shape	Density Perturbation	Magnetic Field
A.....	40	Gaussian	None	None
B.....	40	Gaussian	Positive	None
C.....	40	Gaussian	Negative	None
D.....	40	Triangular	None	None
E.....	25	Gaussian	None	None
F.....	40	Gaussian	None	0.5 mG
G.....	40	"Fat" Gaussian	None	None

3.1. *Evolution of the Velocity Profiles and the Formation of Shocks in a Variable Wind*

Figure 1 illustrates how the velocity perturbation of model A evolves with time. At the beginning of the simulation the velocity perturbation is a Gaussian, but this shape quickly steepens as the fast material in the perturbation overtakes the slower material. The density and temperature at the front of the perturbation increase, and as a result the line emission from [S II] $\lambda\lambda 6716, 6731$ rises sharply at the front of the perturbation. The emissivity of forbidden lines (e.g., [S II]) is proportional to the density of ion, and also depends on the temperature and the electron density. The rear of the perturbation (the portion that initially has $dv/dx > 0$) undergoes a rarefaction as the fast material runs away from the slower flow. The density and temperature in the rarefaction decrease as the flow evolves.

The flow eventually forms a pair of shocks (at time $t = 1.98$ yr in Fig. 1). The forward shock sweeps up the material ahead of the perturbation and the reverse shock slows the high-velocity material in the perturbation. The region between the two shocks grows with time. As expected, the temperature is highest next to the two shocks. However, the emission from [S II] has only a single peak at the position of the forward shock. The reason for this behavior is clear from the density profiles in Figure 1 at $t \gtrsim 3$ yr. The gas that enters the reverse shock must first pass through a rarefaction wave which lowers its density by a factor of ~ 4. Hence, although the postshock temperature is similar for the forward and reverse shocks, the density, and therefore the [S II] emission, is considerably higher behind the forward shock. The peak density occurs between the two shocks, but the emission peaks close to the forward shock because the temperature is highest there. A similar dense shell of material appears in the simulations of Blondin et al. (1989) between the bow shock and the Mach disk at the head of the jet.

A wind that varies in velocity is likely to vary in density as well, although the sense of the density variations is unclear without a detailed understanding of the mechanism that drives stellar jets. The faster portions of the flow may be ejected with a higher density than that of the slower wind (this scenario would resemble a "bullet" model of the outflow), or the mass-loss rate may be more constant, in which case the high-velocity wind will be less dense than the low-velocity wind.

Model B (Fig. 2) shows how a velocity perturbation evolves when it is accompanied by a similar density enhancement, and model C (Fig. 3) follows the evolution of a velocity perturbation within a constant mass-loss flow (i.e., the initial density perturbation is negative). Models B and C resemble model A in that the velocity perturbations steepen and form a pair of shocks, and the rarefaction waves in models B and C are similar to those of model A.

However, the relative shock velocities of the forward and reverse shocks are different from those in model A because of the initial density perturbations in models B and C. The densest material initially moves at the highest velocities in model B, so when the shocks form the forward shock is much stronger than the reverse shock. This behavior also occurs in bullet models (Norman & Silk 1979), where the forward shock (the "bow shock") has a larger shock velocity than the reverse shock (the "cloudlet shock"). When the least dense material initially moves at the highest velocities, as is the case in model

© American Astronomical Society • Provided by the NASA Astrophysics Data System

1993ApJ...409..705H

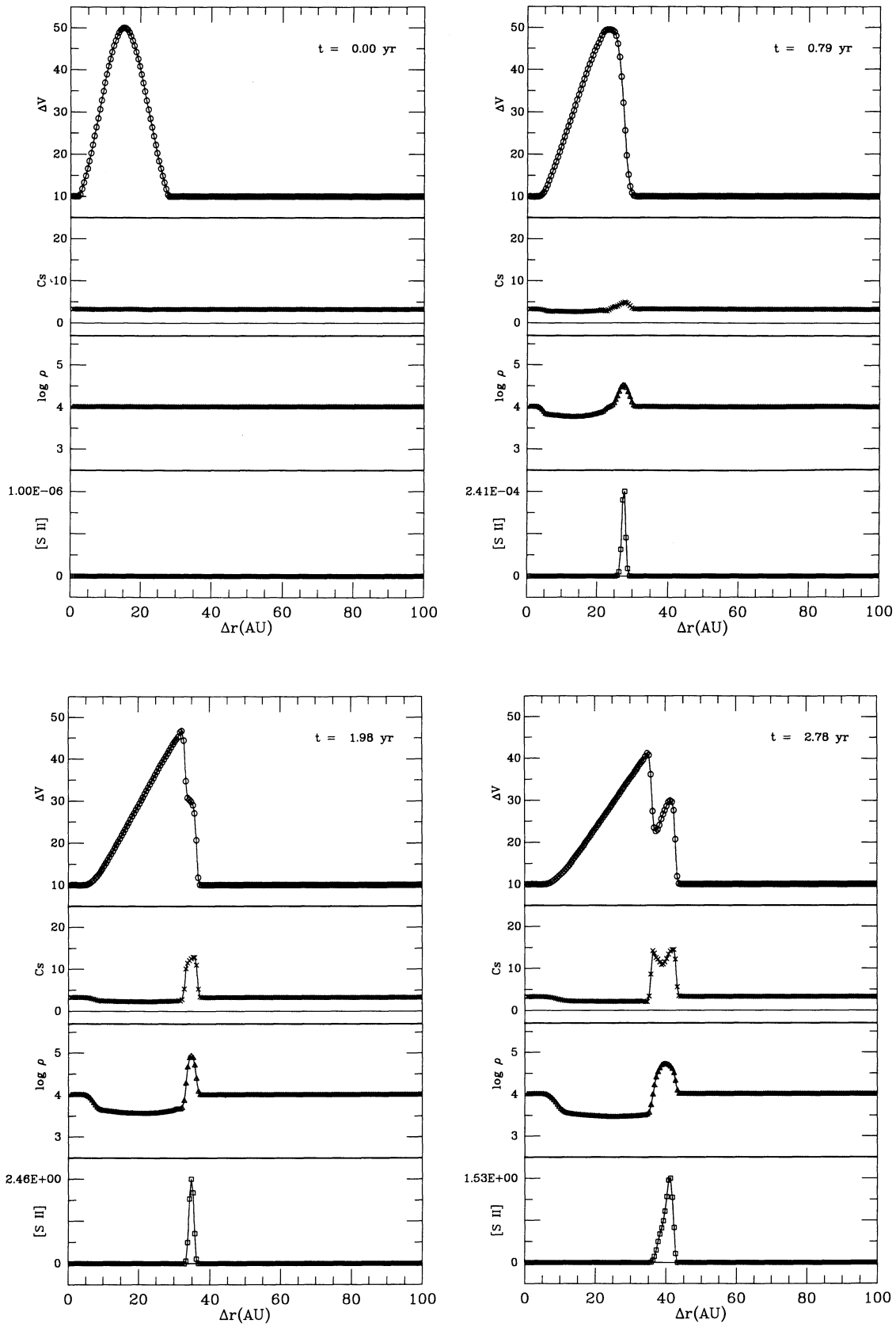

FIG. 1.—Velocity (*circles*, in km s^{-1}), sound speed (*crosses*, in km s^{-1}), log density (*triangles*, cm^{-3}), and log [S II] $\lambda\lambda$6716, 6731 emissivity (*squares*, in 10^{-16} ergs cm^{-3} s^{-1}) are plotted against distance in AU. The models are planar and one-dimensional, so an arbitrary constant may be added to the velocities and distances shown in the figure. The time from the start of the simulation is shown in years. The velocity perturbation is initially Gaussian, and the density is constant. The velocity profile steepens and forms a pair of shocks with equal shock velocities. Dense, hot gas accumulates between the two shocks and gives rise to strong line emission, especially behind the forward shock where the density is largest. Other aspects of the flow are discussed in the text.

© American Astronomical Society • Provided by the NASA Astrophysics Data System

1993ApJ...409..705H

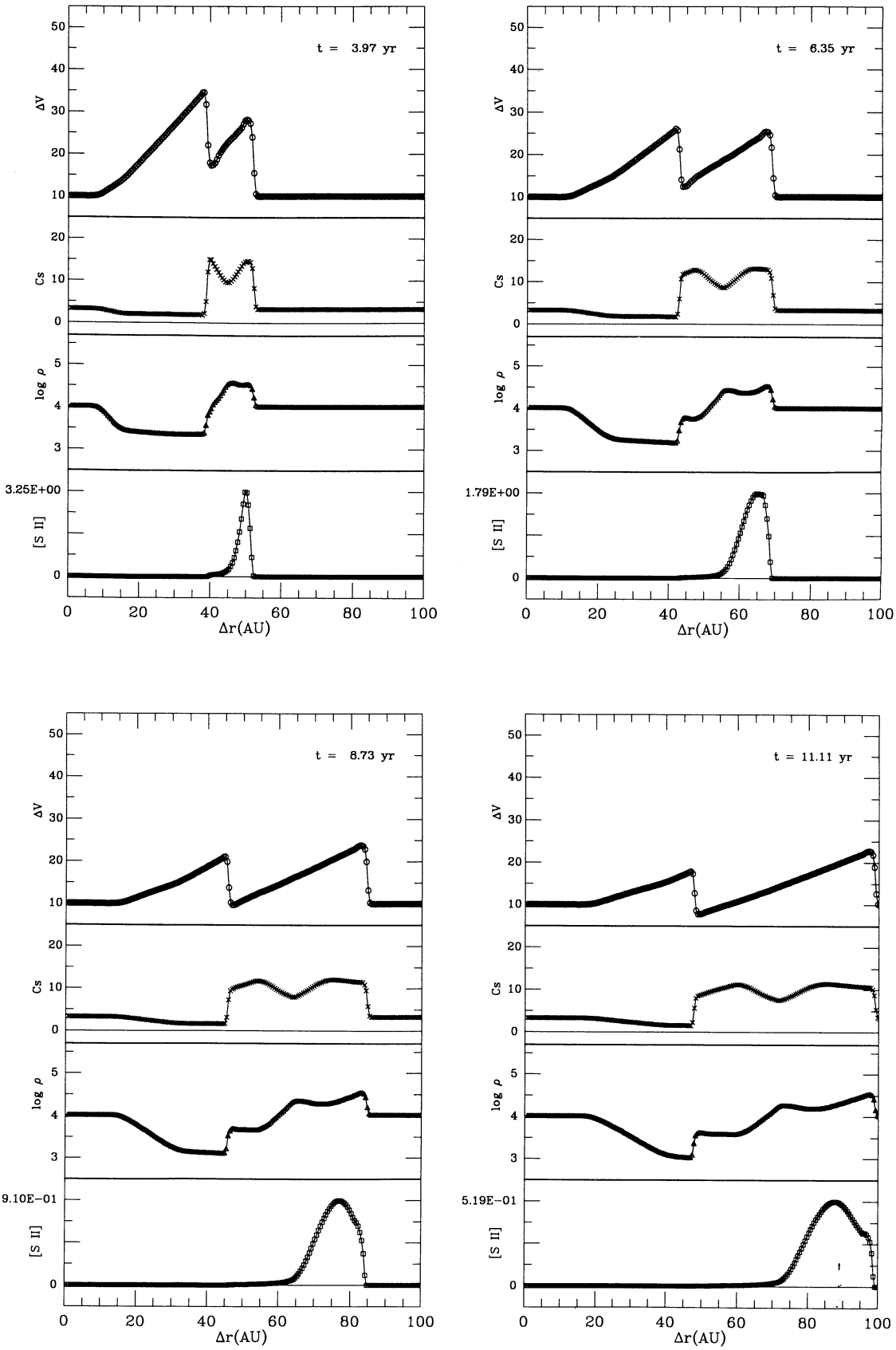

FIG. 1—*Continued*

© American Astronomical Society • Provided by the NASA Astrophysics Data System

1993ApJ...409..705H

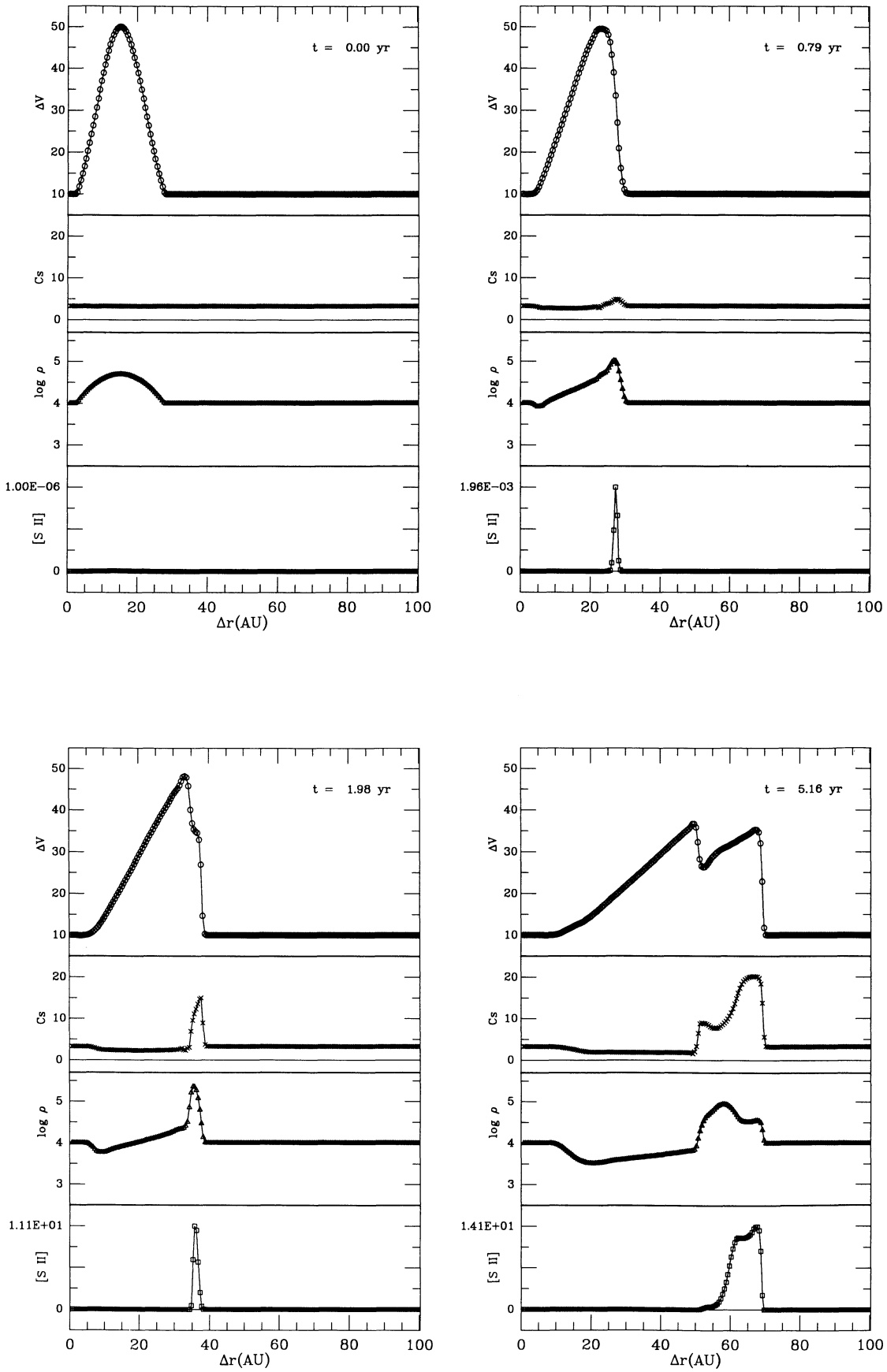

FIG. 2.—Same as Fig. 1 but for Model B, where the velocity perturbation is accompanied by a similar enhancement in the density. This model resembles a "bullet" flow, and forms a forward shock that is stronger (has a larger shock velocity) than the reverse shock.

© American Astronomical Society • Provided by the NASA Astrophysics Data System

1993ApJ...409..705H

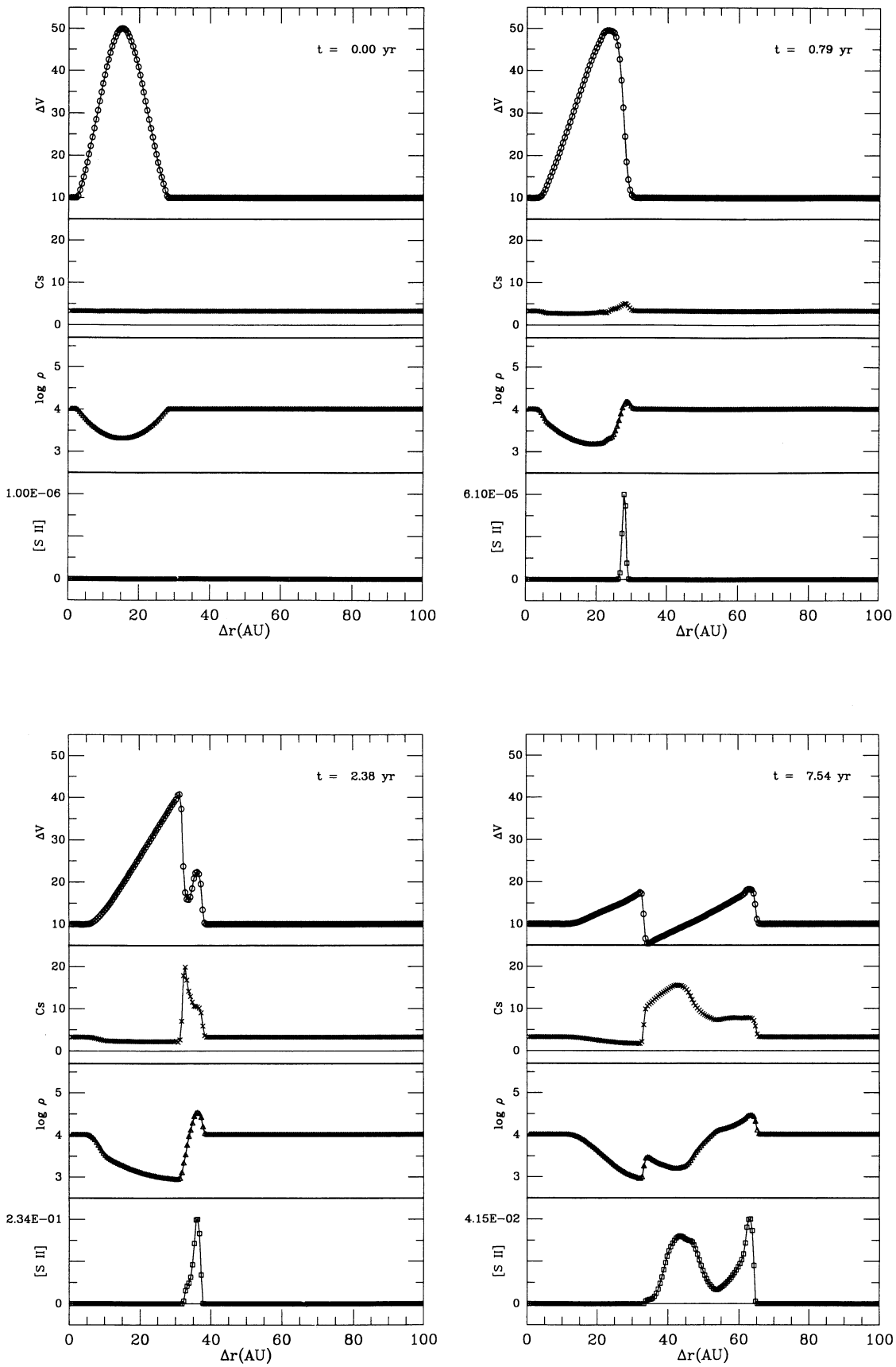

FIG. 3.—Same as Fig. 1 but for Model C, where the velocity perturbation is accompanied by a reduction in the density. In this model the mass-loss rate is constant everywhere in the flow. The low density in the velocity perturbation causes the reverse shock to be stronger than the forward shock, but the larger density behind the forward shock means that the [S II] line emission is comparable from the two postshock regions.

© American Astronomical Society • Provided by the NASA Astrophysics Data System

1993ApJ...409..705H

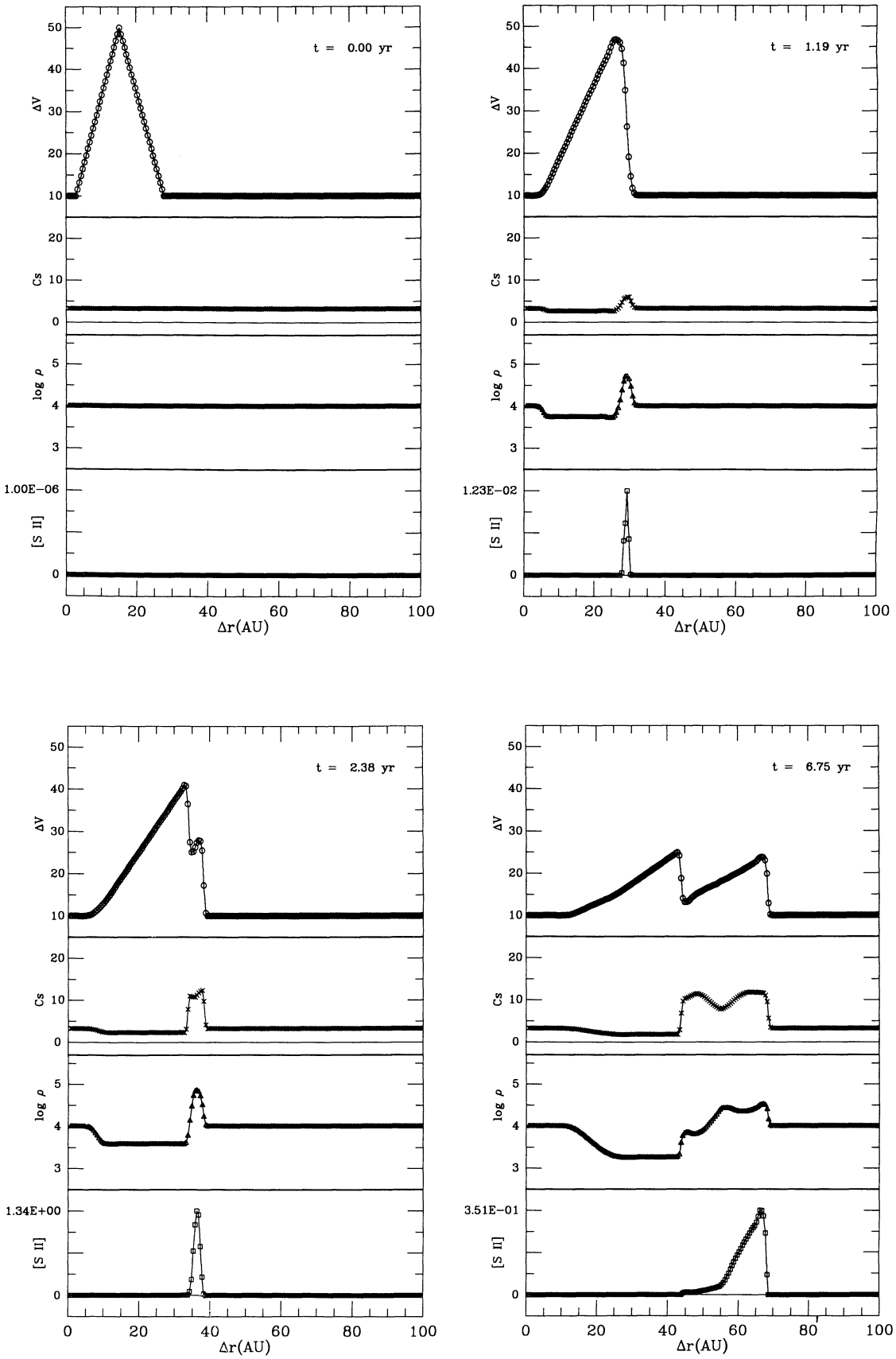

FIG. 4.—Same as Fig. 1 but for Model D. The velocity perturbation is initially triangular in shape

© American Astronomical Society • Provided by the NASA Astrophysics Data System

1993ApJ...409..705H

C, then the reverse shock has a larger shock velocity than the forward shock. Model C resembles a shocked cloudlet model (Schwartz 1978), where the reverse shock (which is the bow shock in the shocked cloudlet model) has a larger shock velocity than the forward shock (the "cloudlet shock").

The higher shock velocity present in the reverse shock in model C offsets the lower density there and makes the reverse shock somewhat brighter than the forward shock in [S II]. The [S II] emission occurs in a single peak behind the forward shock in model B (Fig. 2).

The velocity perturbation in model D (Fig. 4) is triangular in shape, but otherwise this model is identical to model A. As in the other models, the triangular velocity profile in model D steepens (Fig. 4, $t = 1.19$ yr), and forms a pair of shocks (Fig. 4, $t = 2.38$ yr). Once the shocks form, the velocity and density profiles in model D resemble those of the other models closely. The triangular shape means that there is less high-velocity material in model D, so the effective shock velocities and excitation are somewhat lower for this model. Model E (Fig. 5) has a smaller (25 km s^{-1}) velocity perturbation than the other models, and does not differ significantly from model A except that the emission line fluxes from model E are considerably lower than those in model A (see § 3.3).

The collimating agent of stellar jets is highly uncertain, but existing models suggest that magnetic fields may play an important role in this process (e.g., Lovelace, Berk, & Contopoulos 1991). Unfortunately, it is very difficult to measure magnetic fields in HH objects, and the only existing measurement of the magnetic field (~ 20 μG in front of the bow shock in HH 34, Morse et al. 1992) indicates fairly low field strengths. However, there are not as of yet any measurements of magnetic fields within stellar jets, and it is possible that the fields are larger there than in the bow shock region. The magnetic pressure must be comparable to the ram pressure if fields are important in the collimation of the flow, and for stellar jets this means that $B \gtrsim 1$ mG. Much weaker fields suffice to inhibit compression in weak shocks, however, and velocity perturbations will spread out more quickly (at the fast magnetosonic speed) if a magnetic field is present.

Because of the potential interest of magnetic fields in jets, we calculated a model F, which has a large (0.5 mG) transverse magnetic field. Only the perpendicular component of the field will inhibit the compression in our planar models (see Appendix). The velocity perturbation in model F (Fig. 6) dissipates more rapidly than the perturbation in model A and the emission line fluxes and excitations are somewhat lower in model F than they are in model A, but otherwise model F resembles the previous models. The magnetic field limits the compression in the postshock regions, and the density contrast between the forward and reverse shocks is lower than it is in model A. For this reason the reverse shock appears as a separate peak in the spatial distribution of [S II] in model F. Models C and G are the only models where emission from the reverse shock contributes significantly to the total cooling.

3.2. *Line Ratios and Fluxes from the Perturbations*

Figure 7 shows that the total [S II] emission from the models rises quickly on time scales of a year, and then either increases or decreases gradually on time scales of tens of years. In general, the more energetic perturbations are brighter in [S II] and dissipate more slowly than the less energetic perturbations. For example, the [S II] fluxes from the low-velocity perturbation in model E and the constant mass scenario in model C are smaller than those of model A, whereas the [S II] fluxes in the "bullet-like" flow (model B) and in the "fat" perturbation (model G) are larger than the [S II] fluxes of model A. The large magnetic field in model F reduces the total emitted flux because some of the energy that would normally go into heating the postshock gas goes into compressing the field.

The average line fluxes over the first 8 years of the evolution of the perturbations appear in Table 2. These line ratios are what would be expected from the perturbation during the *first few years after the appearance of the knot in the flow*. Even 20–25 km s^{-1} shock velocities produce Hα/[S II] $\gtrsim 1$ during the first few years, although if we average the total emission over a cooling time (several hundred years) we obtain Hα/[S II] < 1 (as in model D20 of Hartigan, Raymond, & Hart-

TABLE 2

EMISSION LINE RATIOS AND FLUXES[a]

Line	A	B	C	D	E	F	G
[S II] Flux[b]	1.0 (−14)	9.8 (−14)	6.7 (−16)	2.5 (−15)	5.5 (−16)	1.4 (−15)	2.1 (−14)
Hα(rec)/Hα(coll)[c]	4.0 (−3)	3.1 (−2)	5.4 (−3)	7.5 (−3)	1.5 (+1)	1.0 (−2)	6.5 (−3)
[S II] λλ6716, 6731	100	100	100	100	100	100	100
Hα	226	490	440	73	2.5	82	330
[O I] λλ6363, 6300	147	134	118	137	126	134	159
[N I] λ5200	89	43	70	84	59	84	85
Mg II λ2800	69	235	52	43	8.3	42	92
[C II] λ2325	40	155	33	23	2.5	22	55
[Fe II] 1.6 μm	24	51	33	27	56	27	27
[O I] λ3727	10	158	22	1.4	0.4	1.3	28
[Si II] 35 μm	15	6.0	118	41	186	64	10
[Fe II] 25 μm	3.1	4.9	18	6.6	29	9.9	2.9
[N II] λλ6548, 6583	3	57	4.8	0.5	0.4	0.5	8.3
[C I] λλ9823, 9850	2.9	2.2	3.2	3.2	4.8	3.2	2.9
[C II] 156 μm	1.2	0.2	15	4.9	22	8.2	0.6
[O I] 63 μm	0.4	0.4	2.5	0.9	4.1	1.4	0.3
He I λ584	0.3	5.6	4.3	0.0	0.0	0.1	0.5

[a] Line ratios and line fluxes averaged over the first 8 years of the simulations listed in Table 1. The line ratios are normalized to [S II] λ6716 + λ6731 = 100.

[b] Flux of [S II] λ6716 + λ6731 at the Earth in units ergs cm^{-2} s^{-1}.

[c] Ratio of Hα caused by recombination to Hα excited by collisions.

© American Astronomical Society • Provided by the NASA Astrophysics Data System

1993ApJ...409..705H

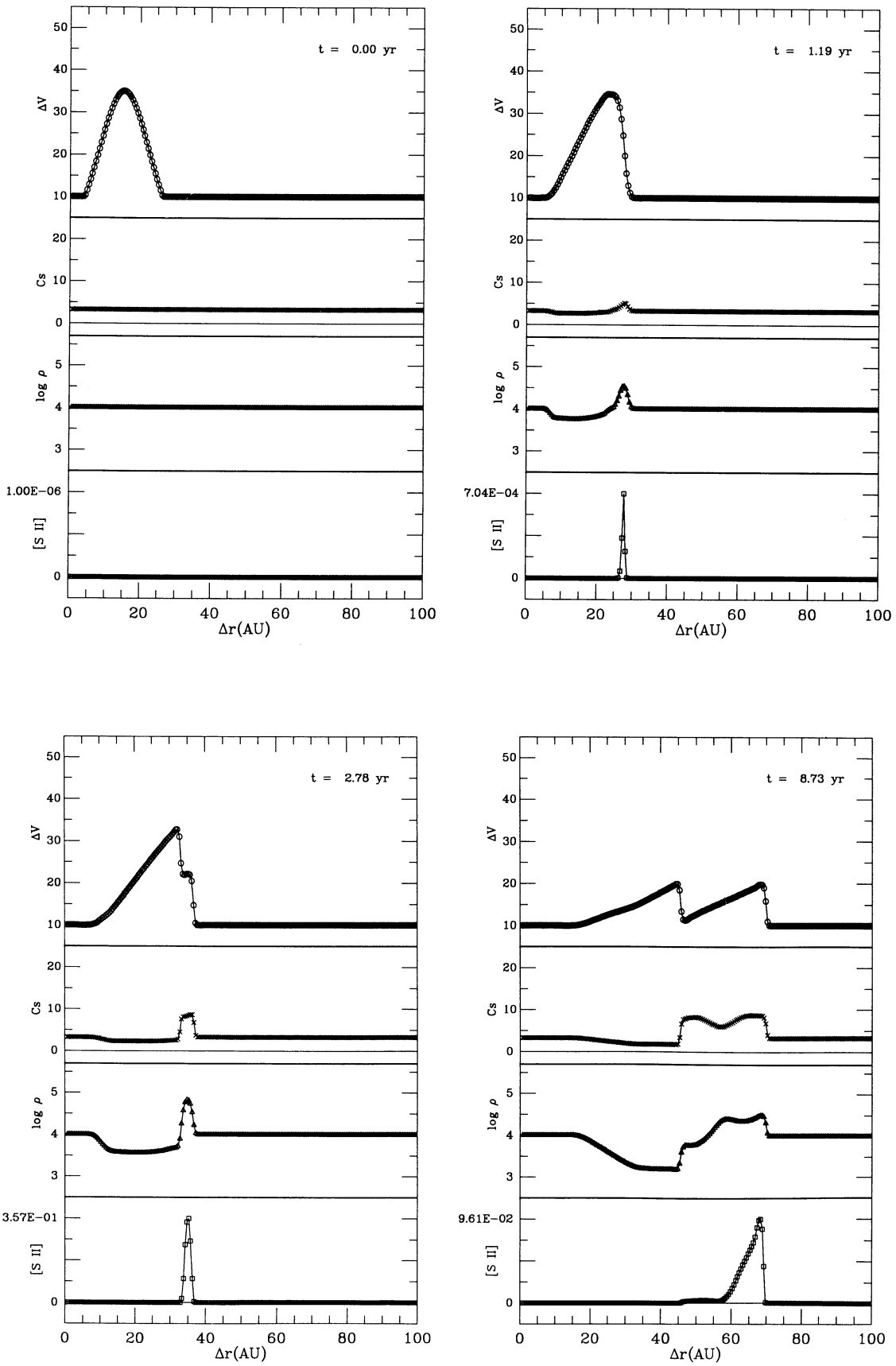

FIG. 5.—Same as Fig. 1 but for Model E. The initial velocity perturbation is only 25 km s^{-1} in this model

© American Astronomical Society • Provided by the NASA Astrophysics Data System

1993ApJ...409..705H

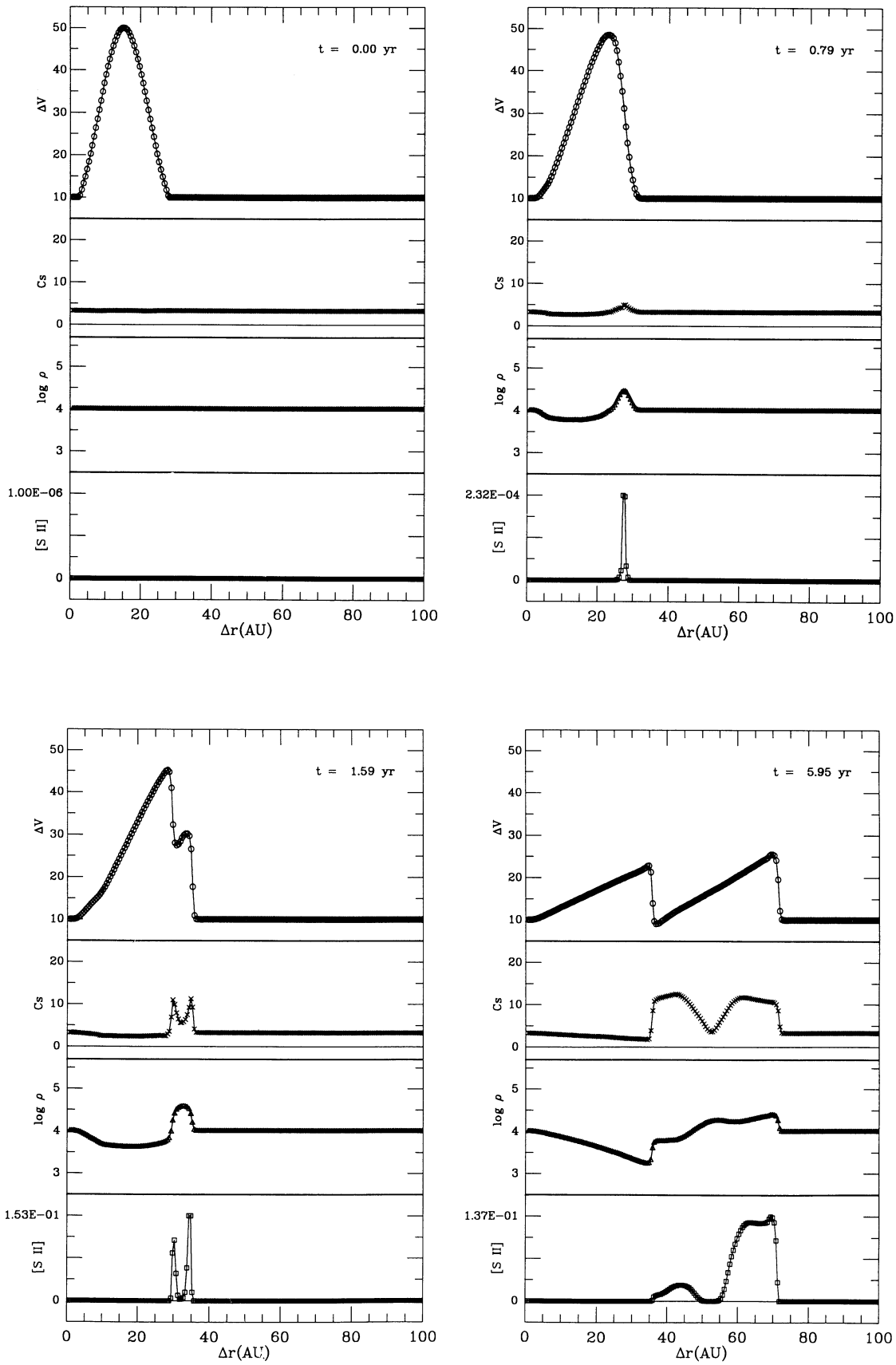

FIG. 6.—Same as Fig. 1 but for Model F, which has an initial magnetic field of 0.5 mG everywhere

© American Astronomical Society • Provided by the NASA Astrophysics Data System

1993ApJ...409..705H

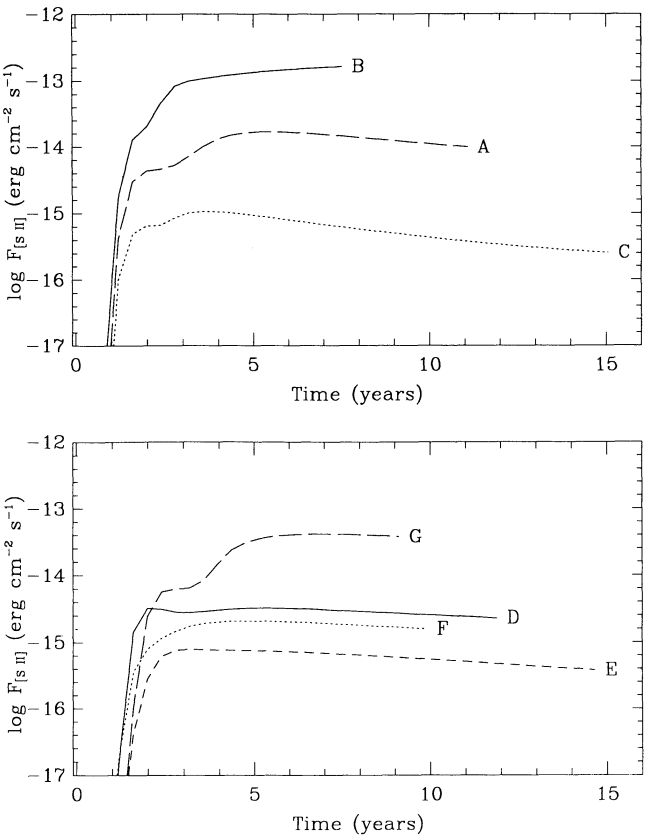

FIG. 7.—Variation of the flux of [S II] λλ6716, 6731 with time for the models listed in Table 1. The flux was calculated from the total [S II] emission over the model, using a jet radius of 2.4 × 10^{15} cm and a distance of 460 pc. The flux rises sharply on a time scale of less than a year and then either increases or decreases gradually over tens of years. A detailed discussion of each model appears in the text.

mann 1987). Most of the Hα emission from these low-velocity shocks comes from collisional excitation. The emission from the compression waves and shocks in our models has a low excitation; that is, the cooling is dominated by low-lying forbidden lines of neutral and singly ionized atoms. The low-energy perturbations (and model F, with the large magnetic field) have a lower excitation spectrum than the high-energy perturbations. The cooling times in our models scale inversely with the preshock density, and the total line fluxes are proportional to the preshock density.

The red doublet lines of [S II] λλ6716, 6731 are usually the brightest lines in optical spectra of stellar jets, and the flux ratio between these two lines allows observers to measure the electron density directly in these flows. We do not calculate the fluxes of the λ6716 and λ6731 separately in our models, but we can predict how the [S II] λ6716/[S II] λ6731 line ratio should vary with time by calculating an average electron density over the entire flow, weighted by the flux of [S II] λ6716 + λ6731 line emission $\{N_e([S\ II]) \equiv \int \epsilon N_e\, dx / \int \epsilon\, dx$, where ϵ is the emissivity of [S II]$\}$.

The average electron density from the red [S II] doublet is shown as a function of time for all seven models in Figure 8. In each model the electron density rises on a time scale of a few years and then varies slowly thereafter. The Gaussian-shaped models without a magnetic field show a momentary decrease in the electron density before the density reaches its maximum value. This decrease is not present in the triangular-shaped model and is caused by the time-dependent behavior of the ionization fraction and the density soon after the forward and reverse shocks form. Generally the electron density inferred from the [S II] line ratio increases as the knot gets brighter, and decreases when the knot fades.

3.3. *The Emission from a Variable Stellar Jet*

The models of variable jets described above make several predictions about line emission that should be possible to test observationally. The shocks in a variable wind move away from the exciting star with a velocity close to that of the wind. Hence, emission knots in a variable wind will always have high radial velocities and large proper motions with respect to the exciting source. Line emission from shocks and compression waves in a variable wind will have a low-excitation spectrum unless the wind varies by enough to produce high shock velocities ($\gtrsim$100 km s^{-1}). On average, knots in variable jets should be more common close to the star because velocity perturbations dissipate after they have formed a shock. This dissipation is evident in our models and those of Stone & Norman (1993), and was also noted independently by Raga (1992) from a study of variable self-similar jets. High proper motions, large radial velocities, low-excitation spectra and proximity to the exciting source are all well-known observed characteristics of stellar jets.

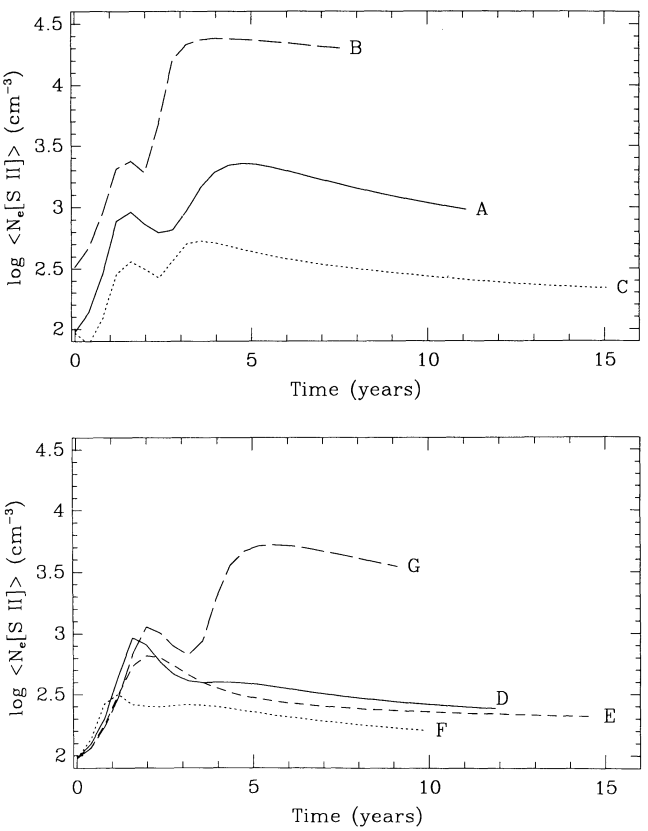

FIG. 8.—Time variation of the electron density that would be measured from the ratio of [S II] λ6716/[S II] λ6731 for the models listed in Table 1. The average electron density generally increases when the knots brighten, and decreases as the knots fade. The magnetic field in model F inhibits the compression and lowers the electron density in the postshock regions.

© American Astronomical Society • Provided by the NASA Astrophysics Data System

1993ApJ...409..705H

Large, closely spaced velocity perturbations will tend to coagulate close to the star, so at large distances from the star we only see the effects of long-term variability of the wind. Two points in the jet with a (supersonic) velocity difference Δv and a separation Δr close to the star will interact with each other after a time $\Delta t \sim \Delta r/\Delta v = R/V_{\rm jet}$, where R is the distance from the star where the points interact and $V_{\rm jet}$ is the velocity of the jet. Hence, only winds that have time scales of variability $\tau = \Delta r/V_{\rm jet} \gtrsim \Delta v \times R/V_{\rm jet}^2$ will still be able to form shocks at a distance R from the star. For a jet like HH 34, $R \sim 10^{17}$ cm, $\Delta v/V_{\rm jet} \sim 0.1$, and $V_{\rm jet} \sim 300$ km s^{-1}, so that $\tau \sim 10$ years. In other words, *the knots formed by velocity changes in a typical stellar jet reflect how much the intrinsic source varies over periods of* $\sim$ *10 years.* Long-term variability ($\sim$100–1000 years) creates multiple bow shocks in stellar jets, and short-term ($\lesssim$1 year) variability of the wind only affects the flow at distances of $\lesssim$100 AU from the star. However, if the velocity amplitude of the short-term variability does not exceed the local magnetosonic sound speed then the short-term velocity variations will produce waves, but not shocks.

Our results show that variable jets can produce a new emission knot in time scales of a few months, with slower long-term variability over decades. The electron density inferred from the ratio of the red [S II] doublet should increase as the knot brightens, and decrease as the knot fades. Unfortunately, existing data on stellar jets are insufficient to address the question of short-term and long-term variability quantitatively.

Recently Eislöffel & Mundt (1992) concluded that entrainment is required to explain the proper motions observed in HH 34. It is possible that both entrainment and variability are important in stellar jets, and it should be possible to distinguish between the two scenarios from observations. When a knot in a variable jet begins to radiate it possesses a large radial velocity and proper motion with respect to the exciting source. In contrast, the proper motion and radial velocity of a knot formed from entrainment should increase from zero to the jet velocity as the knot is accelerated by the jet (Königl 1982). We emphasize that *any* stellar jet that contains supersonic velocity variations will eventually form shocks. The overwhelming evidence (§ 1) that winds from T Tauri stars are highly variable makes it nearly impossible to conceive of a situation where at least some of the emission from stellar jets does not form from a variable wind.

4. SUMMARY

The models we have presented in this paper illustrate how velocity perturbations in a variable jet evolve to form knots of shock-heated gas that have large proper motions, high radial velocities, and low-excitation spectra like those observed in jets from young stars. Shocks in stellar jets may also have other origins, the most likely ones being entrainment of material surrounding the jet or the interaction of the jet with an inhomogeneous preshock medium. Nevertheless, the marked variability of winds from young stars implies that at least some, and probably most of the knots in stellar jets derive from velocity variability in the wind.

The principal conclusions from this work are summarized below:

1. Supersonic velocity perturbations in a flow always steepen and form a pair of shocks as the faster material overtakes the slower material. This process happens in *any* variable jet, and probably occurs frequently in stellar jets.

2. Once the shocks form, the velocity and density profiles in the flow are independent of the shape of the initial velocity perturbation.

3. When a density perturbation accompanies the velocity perturbation, the forward shock is stronger than the reverse shock (similar to a "bullet" of dense material). A velocity perturbation without a density enhancement produces shocks of equal strengths, and gives rise to two distinct temperature peaks.

4. The [S II] emission from the shocks in our models arises primarily from the forward shock in most cases. The forward shock is usually brighter than the reverse shock because material that enters the reverse shock must first pass through a rarefaction wave, which lowers the preshock density. The reverse shock is brighter only if the velocity perturbation is accompanied by a negative density perturbation. The density peak between the two shocks does not always coincide with the position of maximum [S II] emission because forbidden line emission also depends upon the temperature and ionization fraction of the gas.

5. The inclusion of a magnetic field in the models inhibits the compression in the postshock regions, particularly behind the forward shock. The line fluxes and excitation are reduced if there is a strong magnetic field, but the overall appearance of the flow remains unchanged. Velocity perturbations dissipate more quickly when a strong magnetic field is present.

6. Knots in stellar jets that arise from velocity changes in the flow show how much the intrinsic source varies over periods of $\sim$10 years. Long-term variability ($\sim$100–1000 years) of the wind produces multiple bow shocks in stellar jets, and short-term ($\lesssim$1 year) variability of the wind only affects the flow at distances of $\lesssim$100 AU from the star.

7. The total [S II] emission from the shocks produced by the velocity perturbations considered here rises sharply on a time scale of a few months, and then either increases or decreases gradually (depending on the size of the velocity perturbation) over tens of years.

P. H. acknowledges J. Kwan, D. Van Blerkom, and J. Stone, for useful discussions concerning magnetic fields, traffic jams, and variable jets, A. Königl, the referee, for useful comments concerning the presentation of the results, and S. Edwards for her comments on a draft of this paper.

APPENDIX

DESCRIPTION OF THE NUMERICAL MODEL

Our numerical model is a modification of the code described in detail by Yahil et al. (1985, hereafter YJB). The YJB code employs Godunov's method in a Lagrangian differencing scheme with parabolic spatial accuracy, and has much in common with the models of Woodward & Colella (1984). We have modified the code by constructing an Eulerian remapping routine, and by adding in detailed cooling and a magnetic field. The YJB model is one-dimensional with spherical symmetry, which we changed to one-dimensional planar geometry.

© American Astronomical Society • Provided by the NASA Astrophysics Data System

1993ApJ...409..705H

The conservation equations for mass, momentum, and energy are

$$\nabla \cdot (\rho \boldsymbol{v}) + \frac{\partial \rho}{\partial t} = 0 , \tag{A1}$$

$$\frac{\partial \boldsymbol{v}}{\partial t} + (\boldsymbol{v} \cdot \nabla)\boldsymbol{v} = \frac{-\nabla(P + B^2/8\pi)}{\rho} + \frac{(\boldsymbol{B} \cdot \nabla)\boldsymbol{B}}{4\pi\rho} , \tag{A2}$$

$$\frac{\partial}{\partial t}\left(\frac{\rho v^2}{2} + \rho\epsilon + \frac{B^2 + E^2}{8\pi}\right) = -\nabla \cdot \left[\rho \boldsymbol{v}\left(\frac{v^2}{2} + \epsilon + \frac{P}{\rho}\right) + \frac{c}{4\pi}(\boldsymbol{E} \times \boldsymbol{B})\right] + \rho(H - C) , \tag{A3}$$

which reduce in one dimension (planar geometry) to

$$\frac{\partial V}{\partial t} + v\frac{\partial V}{\partial x} - V\frac{\partial v}{\partial x} = 0 , \tag{A4}$$

$$\frac{\partial q}{\partial t} + v\frac{\partial q}{\partial x} = v^2 - \frac{x}{\rho}\frac{\partial(P + B_\perp^2/8\pi)}{\partial x} , \tag{A5}$$

$$\frac{\partial(\rho e)}{\partial t} + \frac{\partial}{\partial x}\left\{\rho v\left[e + \frac{(P + B_\perp^2/8\pi)}{\rho}\right]\right\} = \rho(H - C) , \tag{A6}$$

where we have used $\boldsymbol{E} \times \boldsymbol{B} = c^{-1}\boldsymbol{B} \times (\boldsymbol{v} \times \boldsymbol{B})$, and defined the scalar specific momentum as $q \equiv vx$, the specific volume as $V \equiv \rho^{-1}$, and the specific energy $e \equiv v^2/2 + B_\perp^2/8\pi\rho + \epsilon$; $\epsilon = kT/(\gamma - 1)$ is the specific internal energy. We consider atomic flows, so the ratio of specific heats $\gamma = 5/3$. The heating and cooling per gram are H and C, respectively, and $B_\perp^2 \equiv B_y^2 + B_z^2$.

To change the independent variable from x to a Lagrangian variable m (the enclosed mass) we define $dm = \pi r_j^2 \rho\, dx$. So for any hydrodynamical variable Q

$$\frac{\partial Q(m, t)}{\partial m} = \frac{1}{\pi r_j^2 \rho}\frac{\partial Q(x, t)}{\partial x} , \tag{A7}$$

$$\frac{\partial Q(m, t)}{\partial t} = \frac{\partial Q(x, t)}{\partial t} + v\frac{\partial Q(x, t)}{\partial x} . \tag{A8}$$

Using equations (A4)–(A8) we obtain

$$\frac{\partial V}{\partial t} - \frac{\partial(\pi r_j^2 v)}{\partial m} = 0 , \tag{A9}$$

$$\frac{\partial q}{\partial t} + \frac{\partial[\pi r_j^2 x(P + B_\perp^2/8\pi)]}{\partial m} + v^2 + \frac{P + B_\perp^2/8\pi}{\rho} , \tag{A10}$$

$$\frac{\partial e}{\partial t} + \frac{\partial[\pi r_j^2 v(P + B_\perp^2/8\pi)]}{\partial m} = H - C . \tag{A11}$$

Equations (A9), (A10), and (A11) give the time variation of the variables V, q, and e as a sum of a flux term (the $\partial/\partial m$ term) and a source term. To advance the solution in time we follow the standard Godunov method and use the resolved pressure P^* and the resolved velocity v^* in the flux terms (e.g., Roe 1986). We obtain the resolved pressure and velocity using the Riemann solver of Chorin (1976) described by YJB.

We model the magnetic field as an additional component of $B_\perp^2/8\pi$ to the pressure (see eqs. [A9], [A10], and [A11]). Although this approach is exact for the flux and source terms, it is an inexact approximation to the Riemann solver. Waves from the interfaces of the cells in a planar model (B_y = constant, B_z = constant) will move at the fast magnetosonic speed $(C_s^2 + V_A^2)^{1/2}$. However, the Riemann solver calculates the velocity of the waves as $[\gamma(P + B_\perp^2/8\pi)/\rho]^{1/2} = [C_s^2 + (\gamma/2)V_A^2]^{1/2}$, which is exact only for $\gamma = 2$. For $\gamma = 5/3$, the wave speeds calculated from the approximate Riemann solver will be exact for $B = 0$, and will deviate from the exact solution by a maximum of 9% in the limit of large B. Hence, our approximate Riemann solver should provide an accurate description of the one-dimensional flow. We take the ratio B/ρ as constant throughout the flow.

Because the model is one-dimensional, we can include detailed cooling. We recalculate the ionization fraction at each point between the predictor and corrector steps by solving the non–steady-state ionization and recombination rates in each cell. The line emission consists of recombination plus collisional excitation followed by radiative decay. Collisional excitation and collisional ionization are included in the model, but we neglect photoionization. The abundances and ionization states used are described in the text.

We tested the model in several ways. The first test was to reproduce the Sedov blast wave solution described in YJB. We then tested the Eulerian remap routine by evolving a spherically symmetric wind with constant initial temperature with time. The wind cools at it expands, and it is possible to derive an analytic solution to the final steady-state temperature distribution of the wind with respect to the star. The model converged to the analytic solution without oscillating by means of a rarefaction wave that was strongest at the smaller radii, where the expansion is largest. Finally, we checked to make sure that the planar one-dimensional code gave identical results with the spherical one-dimensional code in the limit that $\delta r/r \ll 1$, and that a constant planar wind did not vary with time.

© American Astronomical Society • Provided by the NASA Astrophysics Data System

1993ApJ...409..705H

REFERENCES

Blondin, J., Königl, A., & Fryxell, B. 1989, ApJ, 337, L37
Bührke, T., Mundt, R., & Ray, T. 1988, A&A, 200, 99
Chorin, A. J. 1976, J. Comput. Phys., 22, 517
Edwards, S., Ray, T., & Mundt, R. 1993, in Protostars and Planets III (Tucson: Univ. Arizona Press), in press
Eislöffel, J., Günther, E., Hessman, F., Mundt, R., Poetzel, R., Carr, J., Beckwith, S., & Ray, T. 1991, ApJ, 383, L19
Eislöffel, J., & Mundt, R. 1992, A&A, in press
Falle, S. 1991, MNRAS, 250, 581
Falle, S., Innes, D., & Wilson, M. 1987, MNRAS, 225, 741
Hartigan, P. 1989, ApJ, 339, 987
Hartigan, P., Kenyon, S. J., Hartmann, L., Strom, S. E., Edwards, S., Welty, A., & Stauffer, J. 1991, ApJ, 382, 617
Hartigan, P., Raymond, J. C., & Hartmann, L. 1987, ApJ, 316, 323
Hartigan, P., Raymond, J., & Meaburn, J. 1990, ApJ, 362, 624
Hartmann, L., Kenyon, S., & Hartigan, P. 1993, in Protostars and Planets III (Tucson: Univ. Arizona Press), in press
Königl, L. A. 1982, ApJ, 261, 115
Landau, L., & Lifshitz, E. 1959, Fluid Mechanics (NY: Pergamon), 369
Lovelace, R., Berk, H. L., & Contopoulos, J. 1991, ApJ, 372, 696
McKee, C. 1974, ApJ, 188, 335
Morse, J., Hartigan, P., Cecil, G., Raymond, J., & Heathcote, S. 1992, ApJ, 399, 231
Mundt, R. 1984, ApJ, 280, 749
Norman, C. A., & Silk, J. 1979, ApJ, 228, 197
Norman, M. L., Smarr, L., & Winkler, K.-H. A. 1985, in Numerical Astrophysics, ed. J. Centrella, J. LeBlanc, & R. Bowers (Boston: Jones and Bartlett), 88
Raga, A. 1992, preprint
Raga, A., Binette, L., & Canto, J. 1990, ApJ, 360, 612
Raga, A., Canto, J., Binette, L., & Calvet, N. 1990, ApJ, 364, 601
Raga, A., & Kofman, L. 1992, ApJ, 386, 222
Reipurth, B. 1989, in Low Mass Star Formation and Pre–Main-Sequence Objects, ed. B. Reipurth (Garching: ESO), 247
Reipurth, B., Bally, J., Graham, J. A., Lane, A. P., & Zealey, W. J. 1986, A&A, 164, 51
Reipurth, B., & Heathcote, S. 1991, A&A, 246, 511
Reipurth, B., Raga, A. C., & Heathcote, S. 1992, ApJ, 392, 145
Roe, P. 1986, Ann. Rev. Fluid Mech., 18, 337
Schwartz, R. D. 1978, ApJ, 223, 884
Stone, J., & Norman, M. 1993, in preparation
Whang, Y. C. 1991, ApJ, 377, 255
Wilson, M. 1984, MNRAS, 209, 923
Wilson, M., & Falle, S. 1985, MNRAS, 216, 971
Woodward, P. R., & Colella, P. 1984, J. Comput. Phys., 54, 174
Yahil, A., Johnston, M. D., & Burrows, A. 1985, STSCI Preprint No. 62

© American Astronomical Society • Provided by the NASA Astrophysics Data System